



X-RAY SPECTRAL AND OPTICAL PROPERTIES OF A ULX IN NGC 4258 (M106)

H. AVDAN^{1,2}, S. AVDAN^{1,2}, A. AKYUZ^{1,2}, S. BALMAN³, N. AKSAKAR^{2,4}, AND I. AKKAYA ORALHAN⁵¹ Department of Physics, Cukurova University, 01330 Adana, Turkey; avdan.hsn@gmail.com² Space Sciences and Solar Energy Research and Application Center (UZAYMER), Cukurova University, 01330 Adana, Turkey³ Department of Physics, Middle East Technical University, 06800 Ankara, Turkey⁴ Vocational School of Technical Sciences, Cukurova University, 01410 Adana, Turkey⁵ Department of Astronomy and Space Sciences, Erciyes University, 38039 Kayseri, Turkey

Received 2015 December 30; revised 2016 June 4; accepted 2016 June 25; published 2016 September 8

ABSTRACT

We study the X-ray and optical properties of the ultraluminous X-ray source (ULX) X-6 in the nearby galaxy NGC 4258 (M106) based on the archival *XMM-Newton*, *Chandra*, *Swift*, and *Hubble Space Telescope* (*HST*) observations. The source has a peak luminosity of $L_X \sim 2 \times 10^{39}$ erg s⁻¹ in the *XMM-Newton* observation of 2004 June. Consideration of the hardness ratios and the spectral model parameters shows that the source seems to exhibit possible spectral variations throughout the X-ray observations. In the images from the *HST*/Advanced Camera for Surveys, three optical sources have been identified as counterpart candidates within the 1σ error radius of $0''.3$. The brightest one has an absolute magnitude of $M_V \approx -7.0$ and shows extended structure. The remaining two sources have absolute magnitudes of $M_V \approx -5.8$ and -5.3 . The possible spectral types of the candidates from brightest to dimmest were determined as B6–A5, B0–A7, and B2–A3. The counterparts of the X-ray source possibly belong to a young star cluster. Neither the standard disk model nor the slim disk model provides firm evidence to determine the spectral characteristics of ULX X-6. We argue that the mass of the compact object lies in the range $10\text{--}15 M_\odot$, indicating that the compact source is most likely a stellar-mass black hole.

Key words: galaxies: individual (NGC 4258) – X-rays: binaries – X-rays: general

1. INTRODUCTION

Ultraluminous X-ray sources (ULXs) are extragalactic off-nuclear point-like sources with luminosities exceeding the Eddington limit for a $10 M_\odot$ black hole (BH) ($L_X > 10^{39}$ erg s⁻¹) (Feng & Soria 2011). If the emission is isotropic, the compact objects in some of the bright ULXs might be intermediate-mass BHs with masses $\sim 10^2\text{--}10^4 M_\odot$ (Miller & Colbert 2004). Conversely, some ULXs might contain stellar-mass BHs and their high luminosities may arise from supercritical accretion (Shakura & Sunyaev 1973; Poutanen et al. 2007). Recent studies on ULXs showed that stellar-mass BH scenarios are reliable (Liu et al. 2013; Motch et al. 2014; Fabrika et al. 2015). On the other hand, pulsations with an average period of 1.37 s were detected from a ULX in M82 using *NuSTAR* data, which indicates that the compact object in this system is a neutron star (Bachetti et al. 2014). That result has led to the idea that some ULX systems may harbour neutron stars instead of BHs. The nature of the ULX binary systems is still unclear.

Studying the X-ray spectral states and state transitions of ULXs with the help of available multi-epoch data and comparing them with the well-known characteristics of Galactic BH binaries (BHB) are essential tools for understanding the radiative mechanisms of these sources. There are three active states that have been defined for Galactic BHBs: thermal, hard, and steep power law (PL). In the thermal state, a geometrically thin, optically thick accretion disk dominates the emission, while in the hard state the emission is produced by a geometrically thick, optically thin Comptonizing region. The hard state is characterized by non-thermal PL emission with a photon index $1.4 < \Gamma < 2.1$. However, the steep PL state is defined by a softer spectrum having a photon index of $\Gamma > 2.4$ (Remillard & McClintock 2006). In the steep PL or thermal state, most of the Galactic BHBs have higher luminosities than in the hard state. A similar correlation between luminosity and

photon index has been found in ULXs X-1 in NGC 1313 (Feng & Kaaret 2006; Dewangan et al. 2010) and X37.8+54 in M82 (Jin et al. 2010), although there are some ULXs that exhibit the opposite behavior (NGC 1313 X-2, Feng & Kaaret 2006; NGC 4736 X-2, Avdan et al. 2014). Additionally, distinct spectral state transitions have been observed in some ULXs (e.g., NGC 2403 src 3, Isobe et al. 2009; IC 342 X-1, Marlowe et al. 2014).

On the other hand, identification of the optical counterparts of the ULXs may provide valuable information. The optical emission could originate from the donor star and/or the accretion disk via X-ray photoionization (Feng & Soria 2011). The optical counterparts of several ULXs have been found in nearby galaxies using *Hubble Space Telescope* (*HST*) data (Tao et al. 2011 and references therein; Gladstone et al. 2013). Broadband *HST* photometry of the optical counterparts allows constraints to be placed on the mass and spectral type of the companion star (Grisé et al. 2011, 2012; Yang et al. 2011). These constraints could also be defined by studying the environment of the ULX if the system belongs to a stellar cluster or association (Grisé et al. 2011; Poutanen et al. 2013).

In this work, the X-ray spectral properties of the ULX X-6⁶ in NGC 4258 have been studied using archival *XMM-Newton*, *Chandra*, and *Swift* observations. Also the optical counterpart of X-6 has been searched for in the *HST*/Advanced Camera for Surveys (ACS)/WFC archival images. NGC 4258 (M106) is a nearby (7.7 Mpc, Swartz et al. 2011) Seyfert-type spiral galaxy. It is well known for its anomalous arms, discovered on the basis of H α imaging (Wilson et al. 2001). X-6 is located $2''.4$ away from the center of the galaxy and its *Chandra* coordinate is R.A. = $12^h18^m43^s.887$, decl. = $+47^\circ17'31''.81$. The source

⁶ We adopted the source number from the work of Akyuz et al. (2013). They numbered the detected sources in NGC 4258 as XMM- n , where n represented the source number with decreasing EPIC pn count rate. We have shortened their designation to X-6 for convenience.

Table 1
XMM-Newton, Chandra, and Swift Observations

	Label	ObsID	Date	Good Exp. (ks)
<i>XMM-Newton</i>	XM1	0110920101	2000 Dec 8	16
	XM2	0059140101	2001 May 6	9
	XM3	0059140201	2001 Jun 17	10
	XM4	0059140401	2001 Dec 17	12
	XM5	0059140901	2002 May 22	14
	XM6	0203270202	2004 Jun 1	47
	XM7	0400560301	2006 Nov 17	59
<i>Chandra</i>	C1	1618	2001 May 28	21
<i>Swift</i> XRT	S1	00037259001	2008 Mar 1	10
	S2	00037317001	2008 May 6	3
	S3	00037317002	2009 Mar 9	4
	S4	00037317003	2009 May 9	2
	S5	00037259002	2014 May 21	2
	S6	00037259005	2014 May 24	1
	S7	00037259006	2014 May 25	2
	S8	00080599001	2014 May 25	2
	S9	00037259007	2014 May 30	2
	S10	00037259009	2014 Jun 8	2
	S11	00037259011	2014 Jun 18	0.03
	S12	00037259012	2014 Jun 22	2

was classified as a ULX by Swartz et al. (2011) with an unabsorbed X-ray luminosity of $1.6 \times 10^{39} \text{ erg s}^{-1}$ in the 0.3–10 keV energy band. X-6 is not positionally coincident with any X-ray point source in the *Einstein* and *ROSAT* catalogs. Akyuz et al. (2013) also studied the X-ray spectrum and the temporal properties of this source. They presented spectral and timing analyses based on the *XMM-Newton* observations with the longest exposure available for the non-nuclear X-ray point sources in the D_{25} of NGC 4258.

The paper is organized as follows: the observations and data reductions are described in Section 2. The details and results of the analyses are given in Section 3. Discussion of the physical properties of the ULX and a summary are given in Section 4.

2. OBSERVATIONS

2.1. X-Ray Data

NGC 4258 X-6 was observed multiple times with *XMM-Newton*, *Chandra*, and *Swift* over 14 years. We have reanalyzed all seven *XMM-Newton*, one *Chandra*, and 12 *Swift* observations that are listed in Table 1 with labels, IDs, dates, and good exposures, which indicate exposure times after the removal of background flares. Only observation XM7 was affected by high background flaring, which were excluded from the data (last ~ 3 ks).

XMM-Newton data reductions were carried out using the SAS (Science Analysis Software, version 13.05).⁷ EPCHAIN and EMCHAIN tasks were used to obtain EPIC pn and MOS event files for each observation. The events corresponding to $\text{PATTERN} \leq 12$ and $\text{PATTERN} \leq 4$ with $\text{FLAG} = 0$ were selected for EPIC MOS and pn cameras, respectively. The source and background spectra were extracted with the EVSELECT task using appropriate circular regions of $15''$. The

Table 2
Log of HST/ACS Observations

Filter ^a	Data Set	Date	Exposure (ks)
F435W	JB1F87JHQ	2010 May 30	0.360
F555W	JB1F87010	2010 May 30	0.975
F814W	JB1F87JEQ	2010 May 30	0.360
F606W	J96H27020	2005 Mar 7	1.014
F606W	J96H28020	2005 Mar 9	1.014
F606W	J96H29020	2005 Mar 10	1.014

Note.

^a Bandwidths of filters are $\lambda 3610\text{--}\lambda 4860 \text{ \AA}$ for F435W, $\lambda 4584\text{--}\lambda 6209 \text{ \AA}$ for F555W, $\lambda 4634\text{--}\lambda 7180 \text{ \AA}$ for F606W, and $\lambda 6885\text{--}\lambda 9647 \text{ \AA}$ for F814W.

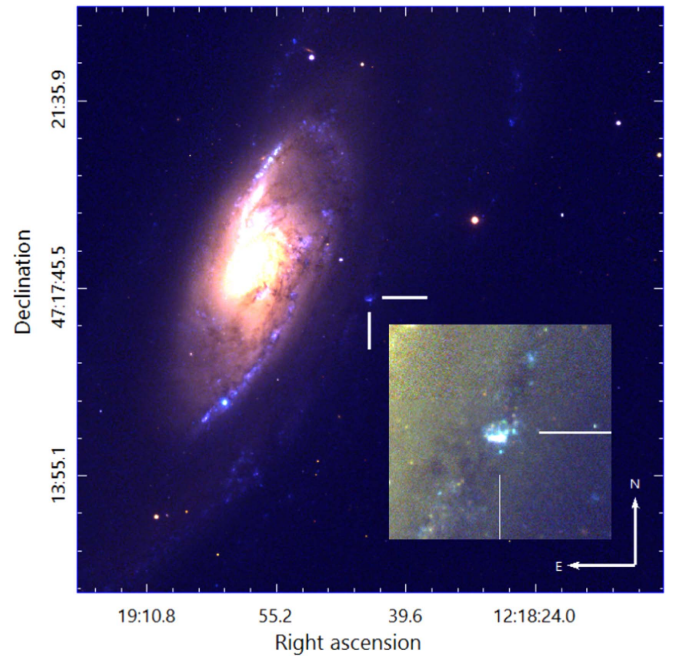


Figure 1. Three-color optical SDSS image of NGC 4258. Red, green, and blue colors represent the SDSS i, r, and u bands, respectively. The white lines shows the bright cluster hosting the ULX.

background regions were selected from a source-free region on the same chip as the source.

Chandra data reductions were performed using the CIAO (*Chandra* Interactive Analysis of Observations, version 4.6) software with the CALDBpackage (version 4.5.9).⁸ The source was located on the ACIS-S3 (back-illuminated) chip. We obtained the level 2 event files using CHANDRA_REPRO script. The SPEXTRACT and DMEXTRACT tasks were used to generate spectrum and light-curve files using circular regions of $10''$. Background photons were extracted by selecting source-free circular regions near the source.

Swift XRT data extractions were done with XSELECT software (version 2.4).⁹ The source and background photons were extracted using circular regions of $20''$. We detected the source in the majority of the *Swift* data sets, but it was not detected in two observations (S3 and S11). The statistical

⁷ <http://xmm.esac.esa.int/sas/>

⁸ <http://cxc.harvard.edu/ciao/>

⁹ <https://heasarc.gsfc.nasa.gov/ftools/xselect/>

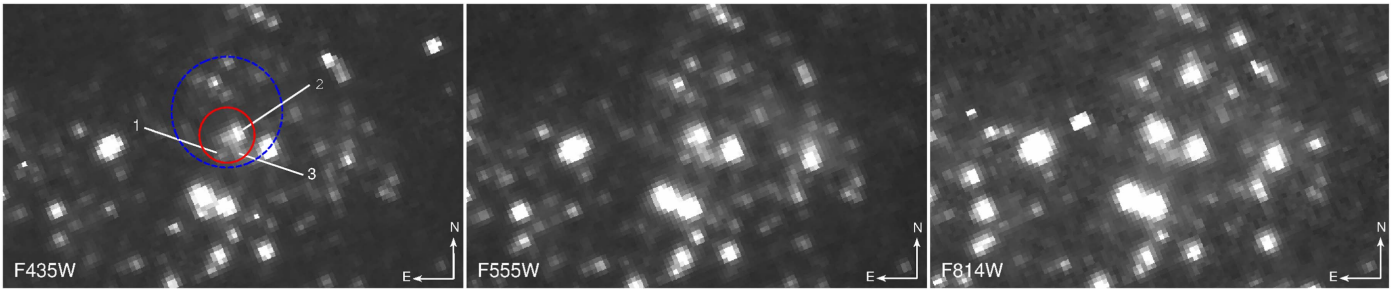


Figure 2. *HST*/ACS images of the region around NGC 4258 X-6 with three filters. The images have a size of $\sim 5'' \times 3''$. The blue dashed circle represents the original *Chandra* position with an accuracy of $0''.6$ and the red circle represents the corrected position with an accuracy of $0''.3$. Three possible counterparts (sources 1–3) are found within the error radius.

quality of the data was not adequate to perform a spectral analysis.

2.2. Optical Data

Observations in the *HST*/ACS/WFC data archive were used to look for the optical counterpart of X-6. A summary of *HST* observations used in this study is given in Table 2. The three-color optical image of NGC 4258 from the Sloan Digital Sky Survey (SDSS) is shown in Figure 1.

In *HST*/ACS/WFC images, the ULX counterpart appears in a star cluster. The relative astrometry between *Chandra* and *HST* was improved to determine the position of the optical counterpart accurately. C1 data and *HST*/ACS/WFC F435W, F555W, and F814W drizzled images were used for astrometric correction. We performed source detection using DAOFIND in IRAF for *HST* and the WAVDETECT task in CIAO for *Chandra*. Then, the sources detected in these images were compared in order to find reference objects to calculate the relative shift between the *Chandra* and *HST* images.

We found two appropriate reference sources in the F435W image, but only one in the F555W and F814W images because the other was out of the frame. Therefore, the F435W image was adopted for astrometric correction by using these two sources as reference objects. One of the sources is the center of the host galaxy and the other one is a point source (R.A. = $12^{\text{h}}18^{\text{m}}49^{\text{s}}.489$, decl. = $+47^{\circ}16'46''.55$) on the same chip as X-6. They have ~ 2860 and 155 counts in C1 data and hence low statistical positional errors of $\sim 0''.02$ and $\sim 0''.08$, respectively.

After the astrometric correction, the position of the candidate counterpart was derived with a positional error of $0''.3$ as R.A. = $12^{\text{h}}18^{\text{m}}43^{\text{s}}.887$, decl. = $+47^{\circ}17'31''.56$ on the *HST*/ACS/WFC F435W image. The *HST*/ACS/WFC F435W, F555W, and F814W images of NGC 4258 together with the corrected position circle on the F435W image are shown in Figure 2. Three possible optical counterparts are identified for X-6 (sources 1, 2, and 3) within the error radius ($0''.3$). All three sources were detected with signal-to-noise ratios (S/N_s) $\gtrsim 30$. Multiple counterpart candidates have also been reported in NGC 1073 ULX, IC 342 X-1, and M82 X-1 (Kaaret 2005; Feng & Kaaret 2008; Wang et al. 2015).

We have also observed the region of X-6 with the RTT-150 (Russian–Turkish Telescope, 150 cm) at TUG (TUBITAK National Observatory, Antalya, Turkey) to confirm that the star cluster belongs to the host galaxy. Using the $1''.7$ slit width, spectroscopic data of the region were obtained by the Turkish Faint Object Spectrograph and Camera instrument with grism 15 (dispersion of 3 \AA pixel^{-1}). A total exposure of 3600 s was acquired. The standard data reduction steps (bias subtraction,

flat-field correction, wavelength and flux calibrations) were performed using IRAF software (version 2.16.1).¹⁰ Neon lamps were used for wavelength calibration. We calculated the redshift of the region from the observed $H\alpha$ ($\lambda 6563$), $H\beta$ ($\lambda 4861$), $[\text{O III}]$ ($\lambda 5007$ and $\lambda 4959$), $[\text{S II}]$ ($\lambda 6717$ and $\lambda 6731$), and $[\text{N II}]$ ($\lambda 6583$) emission lines. The average of the calculated redshifts is $z \sim 0.0016$. This value is similar to the redshift of NGC 4258 ($z_g = 0.001494 \pm 0.000010$, de Vaucouleurs et al. 1991). This result indicates that the cluster and possible optical counterparts of X-6 may belong to the host galaxy.

3. DATA ANALYSIS AND RESULTS

3.1. X-Ray

Investigation of hardness variability may help to define the states and state transition of the source. Therefore, the events were filtered in three different energy ranges: soft (S) 0.3–2 keV, hard (H) 2–8 keV, and total 0.3–8 keV. Then the net count rates of the ULX were derived for each data set. The *XMM-Newton* EPIC pn data were mostly used to calculate the count rates of the source. However, only EPIC MOS data were used for XM4 data because X-6 was partly on the EPIC pn chip gap. To eliminate the differences in sensitivity, the EPIC MOS count rates obtained for XM4 data and the *Chandra* count rate from C1 data were converted to *XMM-Newton* EPIC pn count rates. The conversions were done with the *Chandra* PIMMS toolkit¹¹ by using the best PL parameters calculated for XM4 and C1 data sets. While converting the *Chandra* count rates, the Cycle-3 calibration files were used. The light curves obtained from *XMM-Newton* and *Chandra* data are given in Figure 3(a) and those from *Swift* in Figure 3(b).

The light curve in Figure 3(a) shows that the count rate of the source in the total and soft bands changes by a factor of ~ 2 and that in the hard band by a factor of ~ 2.5 between 2001 and 2007. In Figure 3(b), since the individual *Swift* count rate has large error bars, the data sets taken in 2008–2009 (S1–S4) and 2014 (S5–S12) were combined and the count rates of X-6 were calculated as ~ 0.0025 and $0.0020 \text{ counts s}^{-1}$ in the energy range 0.3–8 keV, respectively. The combined *Swift* count rates indicate a rather persistent behavior. The hard and soft count rates obtained with combined data sets are presented in Figure 3(b) as well.

The hardness ratios (HR), defined as $\text{HR} = (H - S)/(H + S)$, of X-6 were obtained. The long-term evolution of hardness ratio is given in Figure 3(c). As seen in the figure, X-6 has a

¹⁰ <http://iraf.noao.edu/>

¹¹ <http://cxc.harvard.edu/toolkit/pimms.jsp>

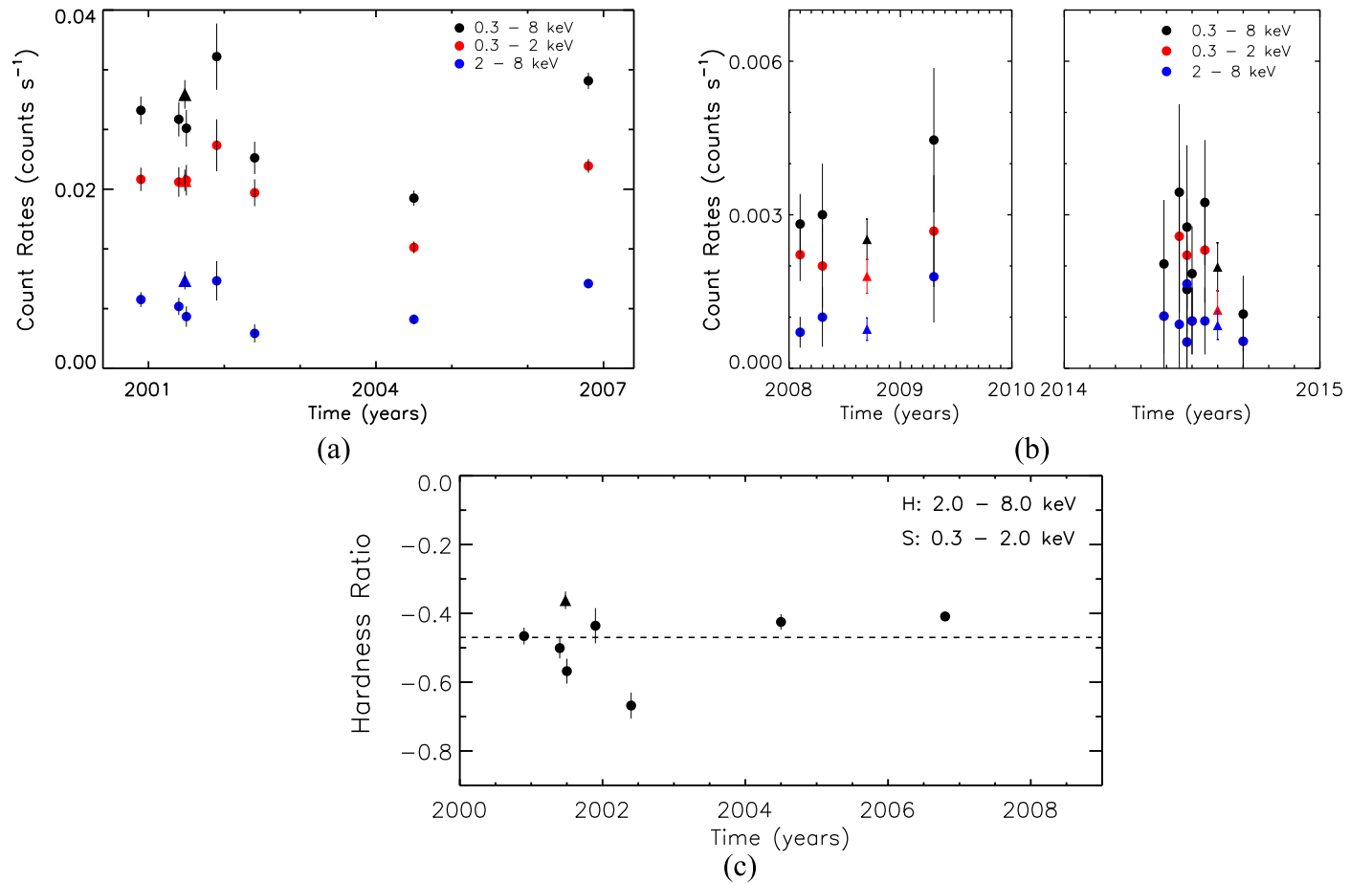


Figure 3. Long-term light curve of NGC 4258 X-6 obtained using (a) *XMM-Newton* and *Chandra* and (b) *Swift* data. The counts were calculated in three energy ranges. In the upper left panel, the filled circles and filled triangle represent *XMM-Newton* and *Chandra* data, respectively. In the upper right panel, the filled circles and filled triangles represent individual and combined *Swift* data, respectively. (c) The long-term hardness evolution of NGC 4258 X-6 calculated with *XMM-Newton* (filled circles) and *Chandra* (filled triangle) data. The horizontal dashed line represents the average value of the hardness ratio calculated from the average count rate of the given energy bands.

noticeably softer HR value in observation XM5 but is nearly constant around the average (~ -0.47) in the other observations. This is in agreement with the fact that the source has the lowest hard count rate in the XM5 data, which are given in Figure 3(a).

The spectral fitting was performed using the *XMM-Newton* and *Chandra* data with XSPEC (version 12.8.1).¹² All spectra were grouped to have a minimum of 20 counts per bin. In the *XMM-Newton* data, the EPIC pn and MOS spectra were fitted simultaneously by including a constant parameter to the fitted models. The constant values that were calculated from the XM7 data set were adopted and fixed while fitting the other *XMM-Newton* observations to achieve consistency. We fitted the 0.3–10 keV spectrum from each *XMM-Newton* and *Chandra* observation using absorbed PL and disk blackbody (DISKBB) models with two absorption components (using tbabs model in XSPEC). One of the absorption components was fixed to the Galactic value ($0.01 \times 10^{22} \text{ cm}^{-2}$; Dickey & Lockman 1990), while the other one was set free to take into account the intrinsic absorption toward the source. The unabsorbed flux values were calculated in the energy range 0.3–10 keV using CFLUX in XSPEC. The spectral results of the fits for individual data sets are given in Table 3. The energy

spectra of the ULX obtained using C1, XM6, and XM7 data are given in Figure 4 for PL and DISKBB models.

Considering the reduced χ^2 values, both PL and DISKBB models provided statistically equivalent fits in XM4 and XM6 data. Also, XM3 data seem better fitted with DISKBB. But for the remaining data sets, the spectra of the source yielded relatively better fits with PL. The analyses revealed that X-6 generally has a hard spectrum ($\Gamma \sim 1.8\text{--}2.1$). However, the spectrum becomes somewhat softer in XM5 data with a steeper photon index of $\Gamma \approx 2.4$ and a lower inner temperature of $T_{\text{in}} \approx 0.8 \text{ keV}$ as derived from PL and DISKBB models, respectively. The calculated flux of X-6 between 0.3 and 10 keV is not constant throughout the observations. The luminosity of the source varies by a factor of 2 and it is in the range $L_X \sim (1.1\text{--}2.2) \times 10^{39} \text{ erg s}^{-1}$ for PL and $L_X \sim (0.5\text{--}1.2) \times 10^{39} \text{ erg s}^{-1}$ for DISKBB models. Furthermore, the absorbed PL+DISKBB composite model was fitted to the spectra. Statistically, the addition of a disk component did not improve the fit significantly.

The energy spectra of some ULXs may show curvature above 2 keV, which is expected from the optically thick corona (Stobbart et al. 2006; Gladstone et al. 2009). Therefore, to search for spectral curvature, we fitted the spectra of X-6 in XM6 and XM7 data with a broken PL model. The modeling gave the best-fit break energies as ~ 2.9 and 3.6 keV ,

¹² <https://heasarc.gsfc.nasa.gov/xanadu/xspec/>

Table 3
X-Ray Spectral Fitting Parameters for X-6

No.	N_H (10^{22} cm^{-2})	Γ	T_{in} (keV)	χ^2/dof	N_{PL}^a (10^{-5})	N_{disk}^b (10^{-3})	L_X^c ($10^{39} \text{ erg s}^{-1}$)	L_{bol}^d ($10^{39} \text{ erg s}^{-1}$)
tbabs*powerlaw								
XM1	$0.10^{+0.03}_{-0.02}$	$1.77^{+0.10}_{-0.10}$...	40.11/33	$2.59^{+0.18}_{-0.18}$...	$1.21^{+0.08}_{-0.09}$...
XM2	$0.21^{+0.04}_{-0.04}$	$2.13^{+0.19}_{-0.19}$...	16.76/17	$3.66^{+0.32}_{-0.32}$...	$1.37^{+0.12}_{-0.11}$...
C1	$0.22^{+0.04}_{-0.04}$	$1.91^{+0.16}_{-0.15}$...	10.39/15	$3.74^{+0.33}_{-0.33}$...	$1.57^{+0.14}_{-0.14}$...
XM3	$0.34^{+0.05}_{-0.04}$	$2.47^{+0.15}_{-0.15}$...	15.67/22	$5.49^{+0.48}_{-0.48}$...	$1.80^{+0.17}_{-0.15}$...
XM4	$0.21^{+0.06}_{-0.04}$	$1.96^{+0.22}_{-0.20}$...	35.13/28	$5.05^{+0.53}_{-0.53}$...	$2.06^{+0.21}_{-0.21}$...
XM5	$0.19^{+0.03}_{-0.03}$	$2.40^{+0.20}_{-0.19}$...	30.49/28	$3.32^{+0.29}_{-0.29}$...	$1.11^{+0.10}_{-0.10}$...
XM6	$0.25^{+0.02}_{-0.02}$	$2.11^{+0.11}_{-0.11}$...	101.26/79	$5.84^{+0.32}_{-0.32}$...	$2.20^{+0.12}_{-0.12}$...
XM7	$0.20^{+0.02}_{-0.02}$	$1.90^{+0.06}_{-0.06}$...	160.34/150	$3.87^{+0.19}_{-0.19}$...	$1.65^{+0.07}_{-0.08}$...
tbabs*diskbb								
XM1	<0.82	...	$1.25^{+0.12}_{-0.10}$	51.67/33	...	$2.21^{+0.16}_{-0.16}$	$0.80^{+0.05}_{-0.06}$	$0.84^{+0.05}_{-0.07}$
XM2	$0.02^{+0.04}_{-0.02}$...	$1.01^{+0.12}_{-0.10}$	19.07/17	...	$4.96^{+0.43}_{-0.43}$	$0.74^{+0.06}_{-0.07}$	$0.78^{+0.08}_{-0.06}$
C1	$0.06^{+0.04}_{-0.03}$...	$1.17^{+0.13}_{-0.11}$	8.18/15	...	$3.48^{+0.30}_{-0.30}$	$0.96^{+0.08}_{-0.09}$	$1.01^{+0.08}_{-0.09}$
XM3	$0.09^{+0.05}_{-0.04}$...	$0.93^{+0.12}_{-0.10}$	20.26/22	...	$7.50^{+0.66}_{-0.66}$	$0.82^{+0.07}_{-0.07}$	$0.87^{+0.06}_{-0.09}$
XM4	$0.01^{+0.05}_{-0.01}$...	$1.23^{+0.17}_{-0.14}$	35.97/28	...	$3.74^{+0.39}_{-0.39}$	$1.23^{+0.14}_{-0.12}$	$1.31^{+0.14}_{-0.13}$
XM5	<0.82	...	$0.83^{+0.10}_{-0.09}$	35.18/28	...	$7.33^{+0.66}_{-0.66}$	$0.53^{+0.05}_{-0.05}$	$0.58^{+0.01}_{-0.09}$
XM6	$0.07^{+0.02}_{-0.02}$...	$1.06^{+0.07}_{-0.07}$	101.28/79	...	$6.87^{+0.37}_{-0.37}$	$1.24^{+0.06}_{-0.06}$	$1.32^{+0.08}_{-0.07}$
XM7	$0.04^{+0.01}_{-0.01}$...	$1.37^{+0.07}_{-0.06}$	174.51/150	...	$2.12^{+0.10}_{-0.10}$	$1.09^{+0.06}_{-0.05}$	$1.15^{+0.06}_{-0.06}$

Notes.

^a Normalization parameter of the PL model in units of $\text{photon cm}^{-2} \text{ s}^{-1} \text{ keV}^{-1}$ at 1 keV.

^b Normalization parameter of the DISKBB model. $N_{\text{disk}} = [(r_{\text{in}} \text{ km}^{-1})/(D/10 \text{ kpc})]^2 \times \cos i$, where r_{in} is the apparent inner disk radius, D is the distance to the source, and i is the inclination of the disk.

^c Luminosity values were calculated using a distance of 7.7 Mpc (Swartz et al. 2011).

^d Bolometric luminosity values were calculated in the energy range 0.01–100 keV.

respectively. However, according to an F-test, the improvement of the fits over the PL model was $<2\sigma$.

A possible iron line was seen in the spectrum of the source in XM6 data. The observation of iron line emission in some ULX spectra could be interpreted to mean that the ULX is in its high state (Strickland & Heckman 2007). This line was fitted with an additional Gaussian line component to the PL model (see Figure 5). The best-fit model parameters for the Gaussian line were $E_{\text{line}} = 6.90^{+0.28}_{-0.12}$ and $\sigma = 0.16^{+0.22}_{-0.15}$. But the iron line is weak and the improvement of the fit was $<2\sigma$. This weak line was not detected in XM7 data, which have a longer exposure. We carried out two tests to check whether the line is associated with the ULX. For the first one, a combined spectrum was obtained by stacking all the pn data of all *XMM-Newton* data to increase the S/N around 7 keV. The line is not significantly detected in the combined spectrum. This is consistent with the possibility that the line emission appears only at certain epochs. For the second test, an image was obtained from pn data that was filtered between 6.6 and 7.5 keV to see whether those few line photons are centered on the position of the source or are spuriously contaminating the source region. The photons seem to center on the source. These results suggest that the iron line (if real) is a variable phenomenon associated with the ULX and not with diffuse emission from gas in the host galaxy.

Additionally, we tried to fit the spectra of X-6 with an absorbed DISKBB model (also known as p -free disk or extended disk blackbody) to interpret the difference between standard disk and slim disk. Disk temperature has a radial dependence as $T(R) \propto R^p$, where p is a free parameter. When

$p = 0.75$ the standard disk model is obtained, and if $p < 0.75$ then radial advection becomes important. The spectral parameters for each observation are given in Table 4. The spectrum of X-6 is well modeled with a p -free model with a p parameter that is indicative of a non-standard disk (~ 0.5), except for C1 data where the model indicated a p parameter consistent with a standard disk. However, we note that the fit statistics are not good enough to distinguish between models. Additionally in XM1, XM2, XM4, and XM5 data the calculated inner disk temperatures (T_{in}) were ≥ 3 keV. Therefore, we fixed the inner disk temperatures to the averaged value (~ 1.70 keV) while fitting these data (see Table 4).

We also calculated bolometric luminosity by integrating the DISKBB model fluxes between energies of 0.01 and 100 keV to obtain a plot of L_{bol} versus T_{in} (see Figure 6). The calculated luminosity values are given in column 9 of Table 3. The plot was fitted with a power-law relation and $L_{\text{bol}} \propto T_{\text{in}}^{1.5 \pm 0.3}$ was found with a correlation coefficient of ~ 0.8 , instead of $L_{\text{bol}} \propto T_{\text{in}}^4$. This relation is expected from an optically thick standard accretion disk (Makishima et al. 2000). Therefore, it seems rather difficult to interpret the emission of ULX X-6 as being the result of a standard disk.

We could not perform spectral fits to the *Swift* data, since the spectral quality was not good enough. However, the maximum 2σ limit on the flux was calculated using the longest *Swift* data (S1) to be $3 \times 10^{-13} \text{ erg cm}^{-2} \text{ s}^{-1}$ by fixing the parameters to the best PL parameters of XM7 data. This corresponds to a luminosity of $L_{0.3-10} \approx 2 \times 10^{39} \text{ erg s}^{-1}$ at the adopted distance.

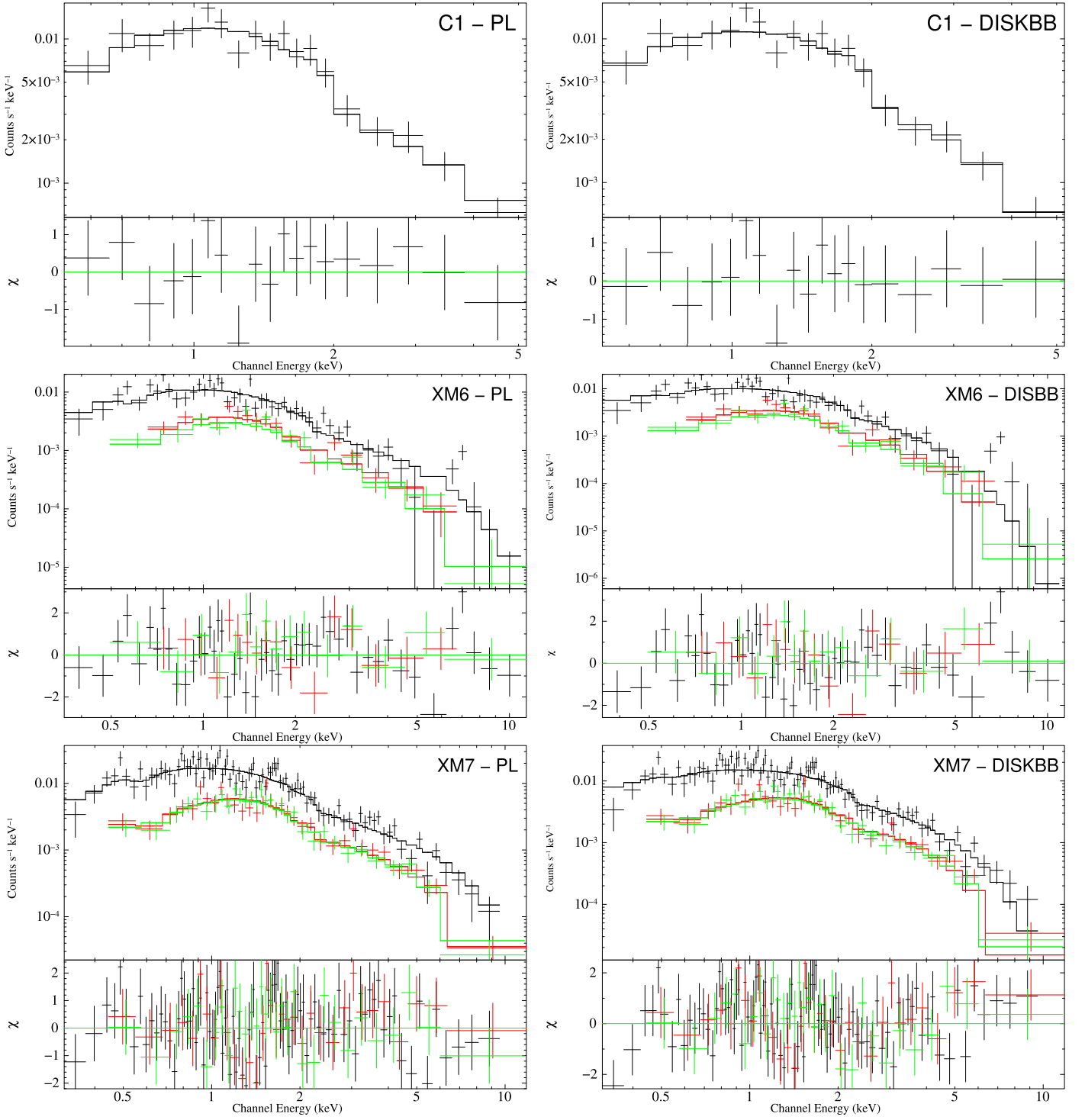


Figure 4. Energy spectra of X-6 obtained using C1, XM6, and XM7 data. In *XMM-Newton* spectra, the black, green, and red data points represent EPIC pn, MOS1, and MOS2, respectively. The fitting models are denoted in the captions of each plot.

We examined the correlation between the best-fit model parameters (given in Table 3) and HR values in order to check the consistency of the fitting parameters. The plots are given in Figure 7. As seen in the upper two panels, the parameters Γ and T_{in} correlate well with HR. However, no correlation could be found between N_{H} values, obtained using PL and DISKBB models, and HR values.

3.2. HST

We have analyzed *HST*/ACS/WFC archival data listed in Table 2 to investigate the optical counterpart of X-6. The position of the ULX on the *HST*/ACS/WFC images was derived as a result of relative astrometric correction (see Section 2.2). There is one relatively bright extended object and another faint object within the error circle. This bright extended

Table 4
X-Ray Spectral Parameters Obtained with the DISKPBB Model

No.	N_H (10^{22} cm^{-2})	T_{in} (keV)	p	χ^2/dof	N_{disk}^a (10^{-4})	L_X^b ($10^{39} \text{ erg s}^{-1}$)
tbabs*diskpbb						
XM1	$0.05^{+0.03}_{-0.02}$	1.70	$0.60^{+0.03}_{-0.03}$	44.17/33	$3.49^{+0.25}_{-0.25}$	$0.92^{+0.06}_{-0.07}$
XM2	$0.16^{+0.04}_{-0.03}$	1.70	$0.52^{+0.03}_{-0.03}$	17.04/17	$1.93^{+0.16}_{-0.16}$	$1.11^{+0.10}_{-0.10}$
C1	$0.05^{+0.04}_{-0.03}$	$1.16^{+0.13}_{-0.11}$	$0.76^{+0.10}_{-0.07}$	8.18/14	$37.39^{+0.33}_{-0.33}$	$0.95^{+0.09}_{-0.08}$
XM3	$0.27^{+0.05}_{-0.04}$	$1.52^{+0.78}_{-0.39}$	$0.50^{+0.02}_{-0.02}$	16.30/21	$2.88^{+0.25}_{-0.25}$	$1.32^{+0.12}_{-0.11}$
XM4	$0.10^{+0.05}_{-0.04}$	1.70	$0.59^{+0.05}_{-0.04}$	35.34/28	$5.29^{+0.55}_{-0.55}$	$1.48^{+0.18}_{-0.14}$
XM5	$0.16^{+0.03}_{-0.03}$	1.70	$0.48^{+0.03}_{-0.02}$	30.86/28	$0.93^{+0.08}_{-0.08}$	$0.94^{+0.09}_{-0.08}$
XM6	$0.18^{+0.02}_{-0.02}$	$1.54^{+0.24}_{-0.19}$	$0.55^{+0.02}_{-0.02}$	99.06/78	$5.96^{+0.32}_{-0.32}$	$1.66^{+0.09}_{-0.09}$
XM7	$0.16^{+0.02}_{-0.02}$	$2.58^{+0.46}_{-0.34}$	$0.55^{+0.01}_{-0.01}$	156.23/149	$0.66^{+0.03}_{-0.03}$	$1.45^{+0.07}_{-0.08}$

Notes.

^a Normalization parameter of the DISKPBB model. $N_{\text{disk}} = [(r_{\text{in}} \text{ km}^{-1})/(D/10 \text{ kpc})]^2 \times \cos i$, where r_{in} is the apparent inner disk radius, D is the distance to the source, and i is the inclination of the disk.

^b Luminosity values were calculated using a distance of 7.7 Mpc (Swartz et al. 2011).

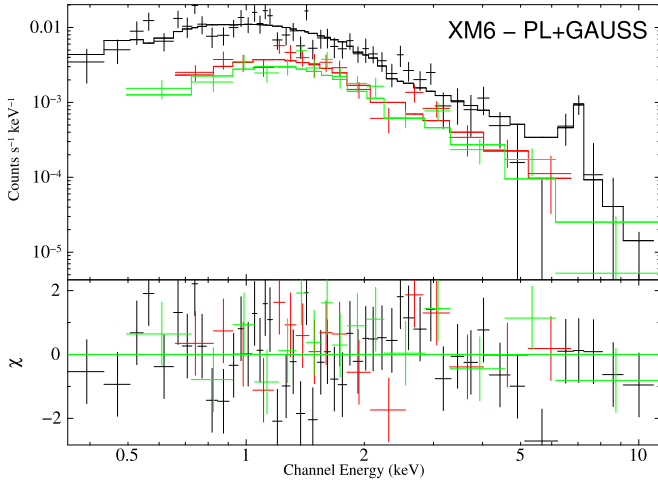


Figure 5. Energy spectrum of X-6 in XM6 data. The spectrum was fitted with an absorbed PL+Gaussian model.

object could also be two stars. By carefully examining the images of F435W and F814W, we considered this possibility and label the three sources within the error circle of X-6 as “source 1,” “source 2,” and “source 3” (see Figure 2). Since the region is crowded, point-spread function (PSF) photometry was performed instead of aperture photometry. Three distinct sources were detected by PSF photometry. Hence, we have analyzed these three sources as possible optical counterparts of X-6.

The PSF photometry was performed with the DOLPHOT software version 2.0 (Dolphin 2000) using the *HST*/ACS/WFC module. The FITS files (*.fit.fits and *.drz.fits) were retrieved from the *HST* data archive.¹³ Standard image reduction algorithms (bias and dark current subtraction, flat fielding) have been applied to the observations. The ACSMASK and SPLITGROUPS tasks were used to mask out all the bad pixels and split the multi-image FITS files into a single file per chip, respectively. Then the DOLPHOT task was used for source detection, photometry, and photometric conversion. The DOLPHOT task gives standard magnitudes using the conversion method as described by Sirianni et al. (2005). This

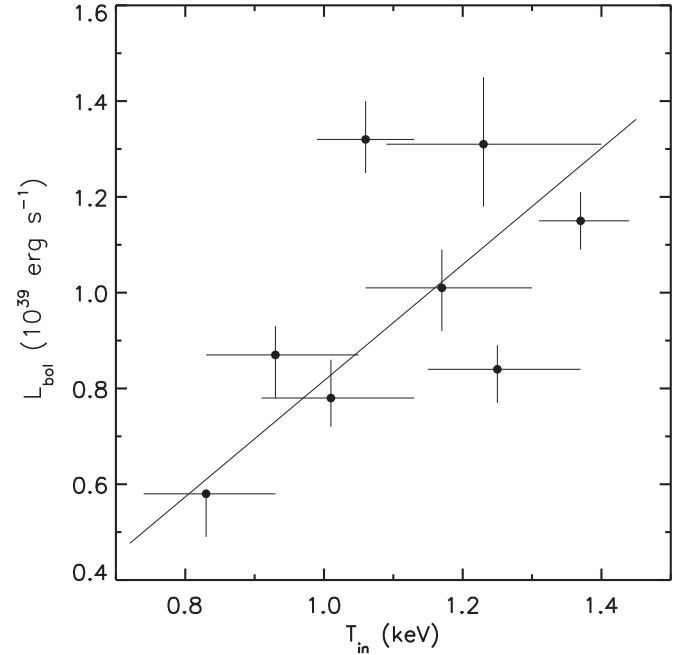


Figure 6. L_{bol} derived from DISKBB models vs. T_{in} . The black line represents the best-fit relation $L_{\text{bol}} \propto T_{\text{in}}^{1.5 \pm 0.3}$ with a correlation coefficient of ~ 0.8 .

task was used for photometry on the images by taking the F435W drizzled image as the positional reference. The Galactic extinction along the direction to NGC 4258 is $E(B - V) = 0.016 \text{ mag}$ (Schlegel et al. 1998). Macri et al. (2006) derived the extragalactic extinction for NGC 4258 in the range of $0.05 \leq E(B - V) \leq 0.28 \text{ mag}$ using 69 Cepheids. The mean extinction obtained from a few Cepheids close to the region around the ULX is $E(B - V) = 0.05 \text{ mag}$. This value is assumed to be more appropriate for the calculation of extinction-corrected magnitudes. Both $E(B - V) = 0.016 \text{ mag}$ and $E(B - V) = 0.05 \text{ mag}$ yielded compatible results. For this reason, we excluded the extinction effect of the galaxy and adopted the Galactic extinction for the reddening correction. The reddening-corrected instrumental VEGA magnitudes, Johnson magnitudes, colors, and absolute magnitudes are listed in Table 5.

¹³ <https://archive.stsci.edu/hst/search.php>

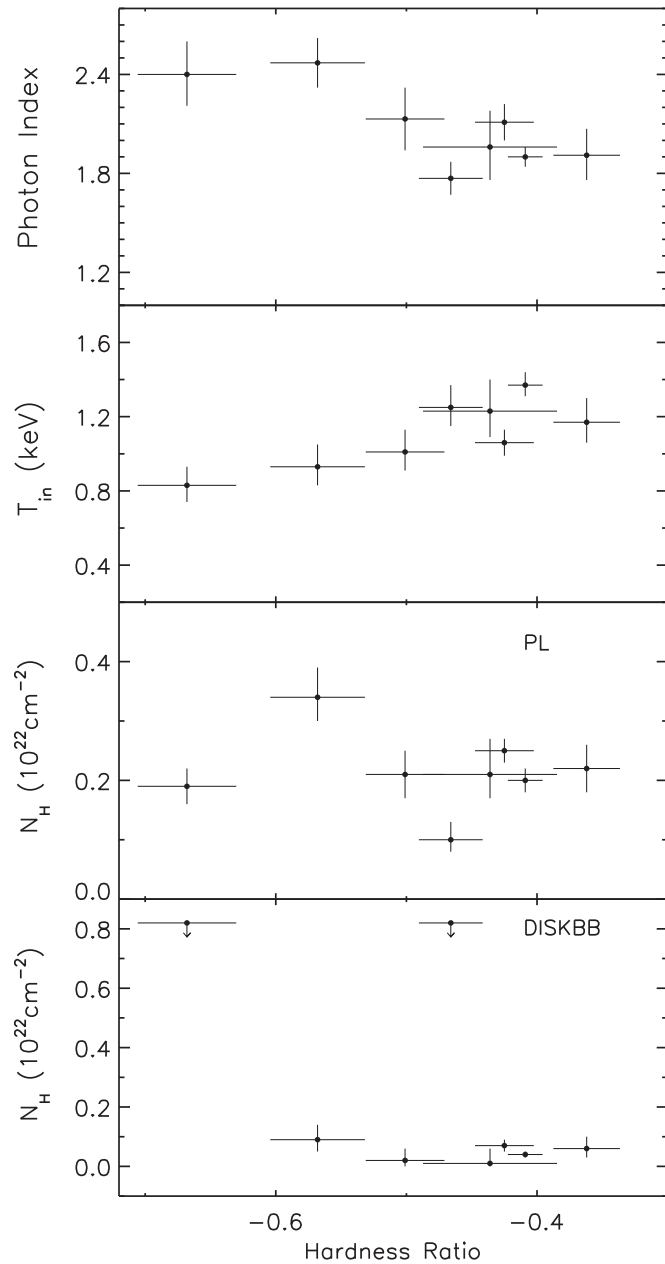


Figure 7. Spectral parameters obtained with PL and DISKBB models vs. hardness ratio (HR).

On the other hand, we also analyzed the *HST*/ACS/WFC F606W archive images to check the optical variability of the counterpart candidates. These observations were performed on 2005 March 7, 9, and 10. The candidates that were found in the other *HST* filters were clearly identified in each observation. The VEGA magnitudes were calculated as 23.592 ± 0.047 , 23.581 ± 0.042 , 23.126 ± 0.032 for source 1, 22.564 ± 0.020 , 22.659 ± 0.021 , 22.616 ± 0.020 for source 2, and 23.001 ± 0.031 , 23.069 ± 0.030 , 23.126 ± 0.032 for source 3. Source 1 shows significant variability ($\Delta m_{F606W} = 0.481 \pm 0.056$), while source 2 and 3 do not show notable variability ($\Delta m_{F606W} < 0.1$).

We obtained two color-magnitude diagrams (CMDs) as F555W versus F435W – F555W and F814W versus F555W – F814W to estimate the age of the sources and the cluster (see Figure 8). For the CMDs, stars within $5''$ radius

Table 5
Magnitude Values of the Three Possible ULX Counterparts Obtained with the *HST*/ACS/WFC Data

Source No.	Filter	VEGA Mag.	Johnson Mag.
Source 1	F435W (<i>B</i>)	24.146 ± 0.046	24.198 ± 0.046
	F555W (<i>V</i>)	24.167 ± 0.048	24.139 ± 0.048
	F814W (<i>I</i>)	24.364 ± 0.073	24.349 ± 0.073
	$(B - V)_0$		0.059 ± 0.066
	$(V - I)_0$		-0.210 ± 0.087
Source 2	M_V		-5.32 ± 0.048
	F435W (<i>B</i>)	22.479 ± 0.017	22.528 ± 0.017
	F555W (<i>V</i>)	22.482 ± 0.017	22.450 ± 0.017
	F814W (<i>I</i>)	22.508 ± 0.022	22.494 ± 0.022
	$(B - V)_0$		0.078 ± 0.024
Source 3	$(V - I)_0$		0.044 ± 0.028
	M_V		-7.01 ± 0.017
	F435W (<i>B</i>)	23.682 ± 0.034	23.732 ± 0.034
	F555W (<i>V</i>)	23.644 ± 0.034	23.617 ± 0.034
	F814W (<i>I</i>)	23.969 ± 0.054	23.953 ± 0.054
	$(B - V)_0$		0.115 ± 0.048
	$(V - I)_0$		-0.336 ± 0.064
	M_V		-5.84 ± 0.034

Note. Extinction-corrected magnitudes were derived in the *HST*/ACS/WFC VEGA magnitude system and in the Johnson–Cousins (*UBVRI*) system.

with $S/N > 4$ were selected. The PARSEC isochrones¹⁴ of Bressan et al. (2012) were used in the CMDs, based on the updated version of the code used to compute stellar tracks. The metallicity of NGC 4258 has been adopted from Kudritzki et al. (2013) as $Z = 0.011$ to obtain the isochrones. The Galactic reddening $E(B - V)$ of this region is given from dust maps as 0.016 according to Schlegel et al. (1998). A distance modulus of 29.4 mag (using the distance of 7.7 Mpc) was used to plot the CMDs. The PARSEC isochrones corresponding to the Z value have been overplotted in Figure 8. The selected nearby bright stars within the $5''$ region have almost the same reddening values, which show that they could be in the same cluster. On the other hand, field stars have different color indices and reddening values. According to the CMDs, we are able to determine the age of the sources and the cluster as < 50 Myr, comparable to the other clusters around ULXs (e.g., Abolmasov et al. 2007; Grisé et al. 2011).

4. DISCUSSION AND SUMMARY

We examined the X-ray temporal and spectral properties of X-6 using seven *XMM-Newton*, one *Chandra*, and 12 *Swift* observations available in the archives. Also, the optical counterpart of X-6 was investigated using archival *HST*/ACS/WFC data. With the help of the simultaneous multi-band *HST*/ACS/WFC data, the CMDs for optical counterpart candidates and the cluster members have been obtained.

As seen in Figures 3(a) and (c), X-6 exhibits possible spectral variations. However, the light curves from the *Swift* data do not show significant variation and indicate a rather persistent behavior (see Figure 3(b)). Most notably, X-6 has the lowest HR value in XM5 data. The source has a steeper PL photon index ($\Gamma \sim 2.40$) and the lowest inner disk temperature ($T_{in} \sim 0.83$ keV) at this epoch. If we assume that the source emits at the Eddington limit in XM6 data (in which the spectrum

¹⁴ <http://stev.oapd.inaf.it/cgi-bin/cmd>

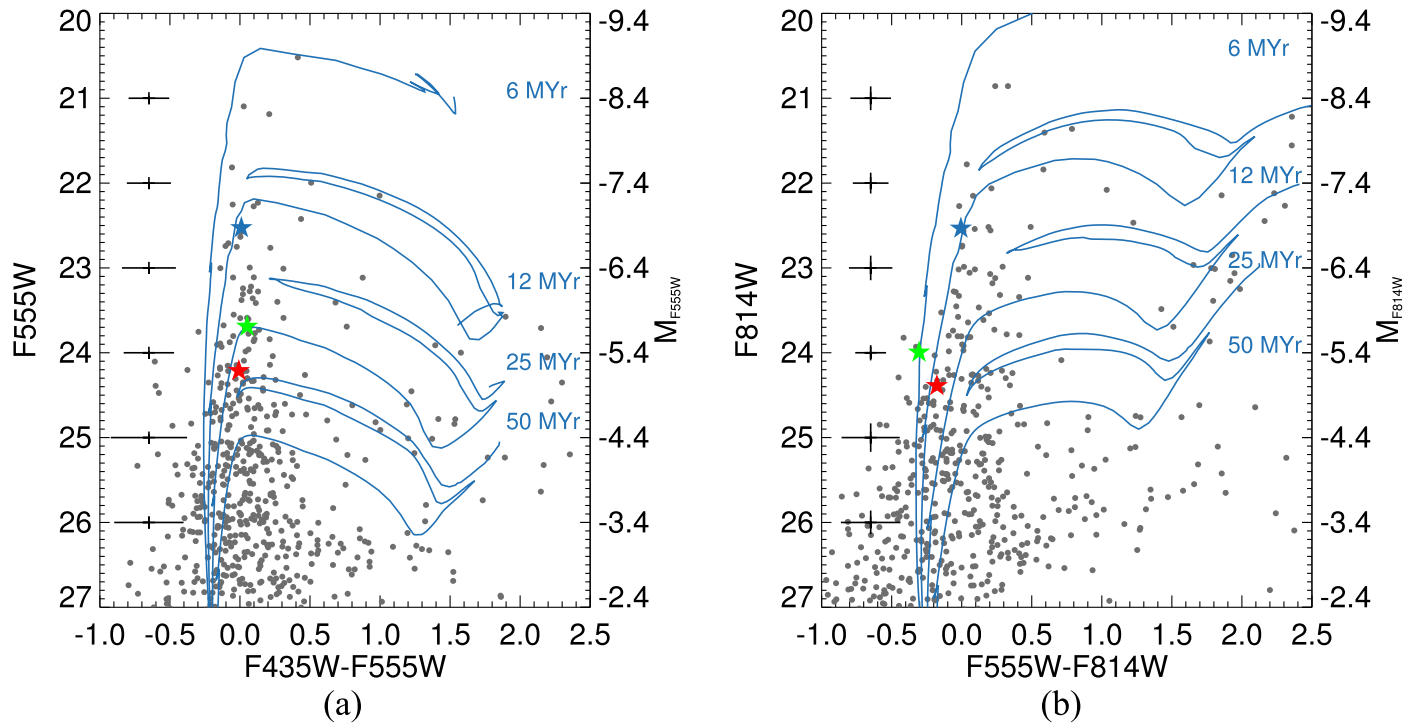


Figure 8. *HST*/ACS/WFC CMDs for the stars in a region of radius 5'' around the ULX counterpart candidates. PARSEC isochrones for different ages and the mean magnitude errors are overplotted. All magnitudes have been corrected for extinction of $E(B - V) = 0.016$ mag. The red, blue, and green stars represent sources 1–3, respectively.

gives the highest $L_X = 2.2 \times 10^{39} \text{ erg s}^{-1}$ the mass of the compact object in this system is found to be $M_{\text{BH}} \sim 15 M_\odot$. The luminosity of X-6 changes by a factor ~ 2 during these variations. Nonetheless, this variation in luminosity seems not to correlate with the canonical BHB states. Generally in Galactic BHBs, the luminosities are usually lower in the hard state, higher in the thermal (soft) state, and switch to a very high value in the steep PL state. However, there are some Galactic BHBs and ULXs that do not show similar behavior (e.g., XTE J1550-564, Remillard & McClintock 2006; NGC 1313 X-2, Feng & Kaaret 2006; IC 342 X-1, Marlowe et al. 2014; NGC 4736 X-2, Avdan et al. 2014).

Taking into account that the ULXs are different than usual Galactic BHBs, each might harbour a stellar-mass BH with a supercritical accretion disk (SCAD) (Fabrika et al. 2015) similar to GRS 1915+105 (Vierdayanti et al. 2010). In the SCAD scenario the disk is expected to be slim ($H/R \sim 1$) within a spherization radius (r_{sp}) and the temperature is expected to depend on the radius as $R^{1/2}$ (Poutanen et al. 2007). We tried to fit the X-ray spectra of X-6 with a p -free model in XSPEC to determine whether X-6 has slim disk properties (Abramowicz et al. 1988; Watarai et al. 2001). The DISKPB model yields acceptable fits to the spectra of the source in C1, XM3, and XM6 data (see Table 4). The p parameters were found to be consistent with the slim disk model with one exception (C1 data, $p \sim 0.75$). This may be due to the decrease in the flux of X-6 in C1 data. The inner disk temperatures obtained from DISKPB fits are consistent with the model (Poutanen et al. 2007) and similar to some other ULXs (e.g., Vierdayanti et al. 2006; Gladstone et al. 2009; Soria et al. 2015).

It is possible to constrain the mass of the compact object using the parameters of the disk models (DISKBB and DISKPB). For this calculation, we used the technique

described by Soria et al. (2015). Since the spectrum of X-6 is relatively better modeled with DISKBB model in XM3 data, the DISKBB normalization parameter obtained using that observation was adopted for this calculation. We found an apparent inner disk radius of $r_{\text{in}} \sqrt{\cos i} \approx 66$ km. The apparent radius was corrected to the true value using the equation $R_{\text{in}} = \xi \cdot \kappa^2 \cdot r_{\text{in}}$, where the correction factor $\xi = 0.412$ and κ is a spectral hardening factor (see Kubota et al. 1998). Assuming $\kappa = 1.7$ (Shimura & Takahara 1995) and a disk inclination $i = 60^\circ$, the true inner disk radius was calculated as $R_{\text{in}} \approx 100$ km. Using the relation between inner disk radius and mass (Makishima et al. 2000), we found a BH mass of $M \sim 10 M_\odot$ for a non-spinning BH.

Also, if we consider the normalization parameter of the DISKPB model in XM3 data, we may calculate another mass value for the compact object. We derived a true inner disk radius of $R_{\text{in}} \sqrt{\cos i} \approx 40$ km using the correction factor $\xi = 0.353$ and a spectral hardening factor $\kappa = 3$ (Vierdayanti et al. 2008). Assuming a moderate disk inclination $i = 60^\circ$ and taking the mass correction factor as minimum (~ 1.2), the mass of the compact object in X-6 can be calculated as $M \sim 10 M_\odot$ for a non-spinning BH. This value is consistent with the estimation in the paragraph above.

Three optical counterpart candidates were identified after the astrometric correction. We calculated the X-ray to optical flux ratios for the three sources. This ratio is given as $\log(f_X/f_V) = \log f_X + m_V/2.5 + 5.37$ where m_V is the extinction-corrected visual magnitude and f_X is the unabsorbed X-ray flux in the energy band 0.3–3.5 keV (Maccacaro et al. 1982). Simultaneous X-ray and optical observations are not available for X-6. Therefore we calculated $\log(f_X/f_V)$ using the minimum (XM5) and maximum (XM6) f_X values adopted from PL model parameters. For source 2, $\log(f_X/f_V)$ was found to be 1.5–1.8. Although these values are within the given ratios for active

galactic nuclei (AGNs) (-1 to 1.7 , Maccacaro et al. 1988), they are acceptable values also for a high-mass X-ray binary. For sources 1 and 3, the ratios were found to be 2.2 – 2.5 and 2.0 – 2.3 , respectively. These ratios are greater than the values for AGNs, normal stars, normal galaxies, and BL Lac objects (Maccacaro et al. 1988; Stocke et al. 1991) and are similar to those for the optical counterparts of other ULXs (Feng & Kaaret 2008; Tao et al. 2011; Yang et al. 2011; Avdan et al. 2016).

Colors and absolute magnitudes of these sources were obtained (see Table 5). These sources have M_V values that are consistent with the optical counterparts of ULXs in Table 4 of Tao et al. (2011), which lie in the range $-7 < M_V < -3$. If we assume that the optical emission of X-6 is dominated by the companion star and we use the Schmidt–Kaler table (Aller et al. 1982) of intrinsic colors, then the probable spectral types of sources 1, 2, and 3 can be estimated to be B2–A3, B6–A5, and B0–A7 supergiants, respectively. We also found, by using the *HST*/ACS/WFC images, that the counterpart candidates of X-6 possibly belong to a star cluster. After obtaining CMDs for the stars in the cluster and using the Padova isochrones, the ages of sources 1, 2, and 3 have been estimated to be in the ranges 15–30, 12–14, and 6–25 Myr, respectively. The masses of the counterpart candidates are estimated from the PARSEC isochrones by taking into account their ages and absolute magnitudes as 9 – $13 M_\odot$ for source 1, 14 – $16 M_\odot$ for source 2, and 10 – $25 M_\odot$ for source 3. The mass ranges of the candidates are compatible with the donor stars of other ULXs (Patruno & Zampieri 2008).

On the other hand, the optical emission could also arise from the accretion disk. When the disk is dominant, this emission is expected to vary significantly, as is found for most ULXs, e.g., M101 ULX-1 (Tao et al. 2011). If the optical variability of the counterpart candidate is taken into account, source 1 is a promising candidate in the present case, and the contribution from the disk cannot be ignored. Therefore, the donor star and the accretion disk may give comparable contributions to the optical emission of X-6.

In summary, even though the source does not exhibit variations in its X-ray spectrum similar to the Galactic BHBs, there are some spectral changes in both HR and spectral model parameters. Nonetheless, it is hard to say anything conclusively about the accretion regime. Additional X-ray data with better statistical quality can constrain the physical parameters better, shedding more light on the origin of the X-ray emission from X-6. Both broadband photometric and high-resolution spectroscopic observations will help to distinguish the optical counterpart and find the origin of the optical emission.

The authors thank the anonymous referee for helpful suggestions that improved the manuscript. We also would like to thank S. Fabrika for his useful comments. This research was supported by the Scientific and Technological Research Council of Turkey (TUBITAK) through project number 113F039. This research is also supported by Cukurova University Research Fund through project number FEF2013D38 and FDK-2014-1998. We thank TUBITAK for a partial support in using RTT-150 (Russian–Turkish 1.5 m telescope in Antalya) with project number 14ARTT150-571.

REFERENCES

- Abolmasov, P. K., Swartz, D. A., Fabrika, S., et al. 2007, *ApJ*, **668**, 124
- Abramowicz, M. A., Czerny, B., Lasota, J. P., & Szuszkiewicz, E. 1988, *ApJ*, **332**, 646
- Akyuz, A., Kayaci, S., Avdan, H., et al. 2013, *AJ*, **145**, 67
- Aller, L. H., Appenzeller, I., Baschek, B., et al. 1982, *Landolt-Bornstein: Numerical Data and Functional Relationships in Science and Technology*, Vol. 2 (New York: Springer)
- Avdan, H., Avdan, S. K., Akyuz, A., & Balman, S. 2014, *Ap&SS*, **352**, 123
- Avdan, S., Vinokurov, A., Fabrika, S., et al. 2016, *MNRAS*, **455**, L91
- Bachetti, M., Harrison, F. A., Walton, D. J., et al. 2014, *Natur*, **514**, 202
- Bressan, A., Marigo, P., Girardi, L., et al. 2012, *MNRAS*, **427**, 127
- de Vaucouleurs, G., de Vaucouleurs, A., Corwin, H. G., Jr., et al. 1991, *Third Reference Catalog of Bright Galaxies* (New York: Springer)
- Dewangan, G. C., Misra, R., Rao, A. R., & Griffiths, R. E. 2010, *MNRAS*, **407**, 291
- Dickey, J. M., & Lockman, F. J. 1990, *ARA&A*, **28**, 215
- Dolphin, A. E. 2000, *PASP*, **112**, 1383
- Fabrika, S., Ueda, Y., Vinokurov, A., Sholukhova, O., & Shidatsu, M. 2015, *NatPh*, **11**, 551
- Feng, H., & Kaaret, P. 2006, *ApJL*, **650**, L75
- Feng, H., & Kaaret, P. 2008, *ApJ*, **675**, 1067
- Feng, H., & Soria, R. 2011, *NewAR*, **55**, 166
- Gladstone, J. C., Copperwheat, C., Heinke, C. O., et al. 2013, *ApJS*, **206**, 14
- Gladstone, J. C., Timothy, P. R., & Done, C. 2009, *MNRAS*, **397**, 1836
- Grisé, F., Kaaret, P., Corbel, S., et al. 2012, *ApJ*, **745**, 123
- Grisé, F., Kaaret, P., Pakull, M. W., & Motch, C. 2011, *ApJ*, **734**, 23
- Isobe, N., Makishima, K., Takahashi, H., et al. 2009, *PASJ*, **61**, 279
- Jin, J., Feng, H., & Kaaret, P. 2010, *ApJ*, **716**, 181
- Kaaret, P. 2005, *ApJ*, **629**, 233
- Kubota, A., Tanaka, Y., Makishima, K., et al. 1998, *PASJ*, **50**, 667
- Kudritzki, R. P., Urbaneja, M. A., Gazak, Z., et al. 2013, *ApJ*, **779**, L20
- Liu, J., Bregman, J. N., Bai, Y., Justham, S., & Crowther, P. 2013, *Natur*, **503**, 500
- Maccacaro, T., Feigelson, E. D., Fener, M., et al. 1982, *ApJ*, **253**, 504
- Maccacaro, T., Gioia, I. M., Wolter, A., Zamorani, G., & Stocke, J. T. 1988, *ApJ*, **326**, 680
- Macri, L. M., Stanek, K. Z., Bersier, D., Greenhill, L. J., & Reid, M. J. 2006, *ApJ*, **652**, 1133
- Makishima, K., Kubota, A., Mizuno, T., et al. 2000, *ApJ*, **535**, 632
- Marlowe, H., Kaaret, P., Lang, C., et al. 2014, *MNRAS*, **444**, 642
- Miller, M. C., & Colbert, E. J. M. 2004, *IJMPD*, **13**, 1
- Motch, C., Pakull, M. W., Soria, R., Grisé, F., & Pietrzyński, G. 2014, *Natur*, **514**, 198
- Patruno, A., & Zampieri, L. 2008, *MNRAS*, **386**, 543
- Poutanen, J., Fabrika, S., Valeev, A. F., Sholukhova, O., & Greiner, J. 2013, *MNRAS*, **432**, 506
- Poutanen, J., Lipunova, G., Fabrika, S., Butkevich, A. G., & Abolmasov, P. 2007, *MNRAS*, **377**, 1187
- Remillard, R. A., & McClintock, J. E. 2006, *ARA&A*, **44**, 49
- Schlegel, D. J., Finkbeiner, D. P., & Davis, M. 1998, *ApJ*, **500**, 525
- Shakura, N. I., & Sunyaev, R. A. 1973, *A&A*, **24**, 337
- Shimura, T., & Takahara, F. 1995, *ApJ*, **445**, 780
- Siriani, M., Jee, M. J., Benítez, N., et al. 2005, *PASP*, **117**, 1049
- Soria, R., Kuntz, K. D., Long, K. S., et al. 2015, *ApJ*, **799**, 140
- Stobart, A. M., Roberts, T. P., & Wilms, J. 2006, *MNRAS*, **368**, 397
- Stocke, J. T., Morris, S. L., Gioia, I. M., et al. 1991, *ApJS*, **76**, 813
- Strickland, D. K., & Heckman, T. M. 2007, *ApJ*, **658**, 258
- Swartz, D. A., Soria, R., Tennant, A. F., & Yukita, M. 2011, *ApJ*, **741**, 49
- Tao, L., Feng, H., Grisé, F., & Kaaret, P. 2011, *ApJ*, **737**, 81
- Vierdayanti, K., Mineshige, S., Ebisawa, K., & Kawaguchi, T. 2006, *PASJ*, **58**, 915
- Vierdayanti, K., Mineshige, S., & Ueda, Y. 2010, *PASJ*, **62**, 239
- Vierdayanti, K., Watarai, K., & Mineshige, S. 2008, *PASJ*, **60**, 653
- Wang, S., Liu, J., Bai, Y., & Guo, J. 2015, *ApJL*, **812**, L2
- Watarai, K., Mizuno, T., & Mineshige, S. 2001, *ApJL*, **549**, L77
- Wilson, A. S., Yang, Y., & Cecil, G. 2001, *ApJ*, **560**, 689
- Yang, L., Feng, H., & Kaaret, P. 2011, *ApJ*, **733**, 118